The Turbulent Structure of the Marine Atmospheric Boundary Layer during and before a Cold Front✐

JIAN HUANG,[d] ZHONGSHUI ZOU,[a,b,c] QINGCUN ZENG,[e] PEILIANG LI,[b] JINBAO SONG,[b] LIN WU,[e] JUN A. ZHANG,[f,g]
SHUIQING LI,[h,i,j] AND PAK-WAI CHAN[k]

[a] *School of Marine Science, Sun Yat-Sen University, Zhuhai, China*
[b] *Ocean College, Zhejiang University, Zhoushan, China*
[c] *Ocean Research Center of Zhou Shan, Zhejiang University, Zhoushan, China*
[d] *Guangzhou Institute of Tropical and Marine Meteorology, CMA, Guangdong, China*
[e] *Institute of Atmospheric Physics, Chinese Academy of Sciences, Beijing, China*
[f] *Cooperative Institute for Marine and Atmospheric Studies, University of Miami, Miami, Florida*
[g] *Hurricane Research Division, NOAA/AOML, Miami, Florida*
[h] *Key Laboratory of Ocean Circulation and Waves, Institute of Oceanology, Chinese Academy of Sciences, Qingdao, China*
[i] *Laboratory for Ocean and Climate Dynamics, Qingdao National Laboratory for Marine Science and Technology, Qingdao, China*
[j] *Center for Ocean Mega-Science, Chinese Academy of Sciences, Qingdao, China*
[k] *Hong Kong Observatory, Hong Kong, China*

ABSTRACT: The turbulent structure within the marine atmospheric boundary layer is investigated based on four levels of observations at a fixed marine platform. During and before a cold front, the ocean surface is dominated by wind sea and swell waves, respectively, affording the opportunity to test the theory recently proposed in laboratory experiments or for flat land surfaces. The results reveal that the velocity spectra follow a k^{-1} law within the intermediate wavenumber (k) range immediately below inertial subrange during the cold front. A logarithmic height dependence of the horizontal velocity variances is also observed above the height of 20 m, while the vertical velocity variances increase with increasing height following a power law of 2/3. These features confirm the attached eddy model and the ''top-down model'' of turbulence over the ocean surface. However, the behavior of velocity variances under swell conditions is much different from those during the cold front, although a remarkable k^{-1} law can be observed in the velocity spectra. The quadrant analysis of the momentum flux also shows a significantly different result for the two conditions.

KEYWORDS: Turbulence; Atmosphere-ocean interaction; Cold fronts; Marine boundary layer

1. Introduction

With high-quality data collected in the boundary layer from both laboratory and field experiments, the turbulent structure has been extensively investigated in the past, reflecting its importance for predicting the exchange of matter and energy at the land/ocean-atmosphere interface. We review findings from previous theoretical studies on the turbulence structure close to the wall and in the atmospheric boundary layer (ABL) over both land and ocean.

a. Attached eddy model of wall turbulence

Based on Townsend's (1976) hypothesis, the attached eddy model (AEM) proposed by Perry and Chong (1982), Perry et al. (1986), Marušić and Perry (1995), and Perry and Marušić (1995) depicts wall turbulence as simple geometrically self-similar attached eddies that respond to the logarithmic velocity profile. Through dimensional analysis and overlap argument,

two self-similar regions in the horizontal velocity spectrum then can be defined: one follows a $k^{-5/3}$ law that is universal for high wavenumbers (k), and the other follows a k^{-1} law that appears only in a region where outer and inner scaled flow overlap.

The k^{-1} law is of particular interest because it corresponds to the main energy-containing eddies. By integrating over the region where the k^{-1} law and inertial subrange hold, a logarithmic variation in the horizontal velocity variances with height is obtained in the same region, where the mean velocity is expected to be logarithmic:

$$\frac{\overline{u_i'^2}}{u_*^2} = B_1 - A_1 \ln\left(\frac{z}{\delta}\right), \quad i = 1, 2; \qquad (1)$$

here, u' represents the horizontal fluctuation after removing the mean wind speed, u_* is friction velocity, δ is the boundary layer thickness, and z is height; $i = 1$ and 2 represent the longitudinal and lateral components of the wind velocity, respectively, and B_1 and A_1 are constants.

Similar analysis of the wall normal component, however, can obtain only the $k^{-5/3}$ law because only eddies of scale $O(z)$ contribute to wall normal motions. As a result, the vertical velocity variance follows:

$$\frac{\overline{u_i'^2}}{u_*^2} = B_2, \quad i = 3, \tag{2}$$

where B_2 is a constant and $i = 3$ represents the vertical component of the wind velocity.

b. Turbulent structure within ABL over land

The AEM is conceived as a model for high Reynolds number flow and thus is suitable for describing the ABL turbulence, owing to the high Reynolds number one or two orders of magnitude larger than that in the laboratory. Compared with laboratory experiments, even though the ABL easily suffers from changes in weather, nonuniform terrain and buoyancy, numerous studies (e.g., Kunkel and Marusic 2006; Hutchins et al. 2012; Pan and Chamecki 2016; Wang and Zheng 2016; Chamecki et al. 2017; Ghannam et al. 2018) have shown that the horizontal velocity spectra in the ABL follow the AEM.

However, the vertical velocity does not follow the AEM of wall turbulence in certain conditions. For instance, Yang and Bo (2018) and Mei and Bo (2019) show that the vertical velocity variances increase slightly with increasing height other than a constant predicted by Eq. (2). To illustrate the turbulence structure within the ABL, Drobinski et al. (2004) suggest that the surface layer (the first 50–100 m of the ABL, where the wind profile follows a logarithmic law and the flux is constant) should be separated into three sublayers: 1) the eddy surface layer (ESL; the first ∼1/10 of the surface layer); 2) the upper surface layer (USL; the upper part of the surface layer); and 3) the shear surface layer (SSL; the intermediate sublayer between ESL and USL). The dynamic processes in the ESL and SSL are different when eddies that originate in the lower part of the ABL impinge on the ground. Because the vertical fluctuations of those eddies are more easily damped than the horizontal fluctuations, the vertical velocity spectra show a k^{-1} range in the SSL but not in the ESL. According to the rapid distortion theory (Townsend 1976), the vertical velocity variances should follow (Högström et al. 2002)

$$\frac{\overline{u_i'^2}}{u_*^2} = B_3 + A_3(z)^{2/3}, \quad i = 3, \tag{3}$$

where B_3 and A_3 are constants. The first term on the right side of Eq. (3) represents shear-generated eddies near the surface, while the second term represents the blocking effect of the surface.

On the other hand, the k^{-1} law always appears in the horizontal velocity spectra in both the ESL and SSL, which is also captured by the "top-down model" proposed by Hunt and Morrison (2000) and Hunt and Carlotti (2001) based on the rapid distortion theory. Besides from k^{-1} and $k^{-5/3}$ laws, studies (e.g., Högström et al. 2002) show that in the low wavenumber range, there is also a third range that follows the +0 power law, so turbulent spectra can be separated into three regimes as follows:

$$E_{ii} \propto \begin{cases} k^{-5/3}, & k \geq a_1 z^{-1} \\ k^{-1}, & a_2 \Lambda^{-1} \leq k < a_1 z^{-1}, \quad i = 1, 2, \\ k^{+0}, & k < a_2 \Lambda^{-1} \end{cases} \tag{4}$$

where Λ is the length scale of the largest eddy and a_1 and a_2 are constants of $O(1)$. Similar to the AEM, the logarithmic variation in horizontal velocity variances with height as expressed in Eq. (1) can be obtained according to Eq. (4). Hence, the k^{-1} law and logarithmic height dependence of the velocity variances are equivalent.

c. Marine atmospheric boundary layer

The turbulence in the marine ABL is more complex than that over a wall or a flat land surface due to the ocean surface waves (Sun and French 2016). Studies (e.g., Hristov and Ruiz-Plancarte 2014; Buckley and Veron 2016) have shown that, in addition to those from shear and buoyancy-generated turbulence predicted by Monin–Obukhov similarity theory (MOST), there are perturbations excited by surface waves in the lower part of the surface layer. Those perturbations can absorb energy from the ABL or exert upward momentum from the ocean to the atmosphere, depending on the wave age and relative angle between the wind stress and wave direction (Grachev and Fairall 2001; Grachev et al. 2003; Högström et al. 2009; Chen et al. 2018; Zou et al. 2019).

The wave boundary layer (WBL) is defined as a layer significantly affected by surface waves. Within the WBL, because wave-induced perturbations carry part of the total stress, the shapes of wind profiles deviate from those over a wall or flat land surface. That is, they may not follow the logarithmic law or MOST (Babanin et al. 2018; Voermans et al. 2019). Under swell conditions, when the momentum flux transfers from the ocean to the atmosphere, the wind profiles have a jet on the upper edge of the WBL, with a positive wind gradient below the jet and negative wind gradient above the jet (Smedman et al. 2009; Högström et al. 2013; Jiang et al. 2016; Zou et al. 2018).

Instead of the k^{-1} law in the intermediate range of the velocity spectra, a swell-related spectra peak is widely reported in field experiments (e.g., Högström et al. 2015; Zou et al. 2019). The swell-related spectra peak is located at the frequency of the dominant waves and corresponds to the influence of wave-induced perturbations. The magnitude of this peak decays exponentially with increasing height, but the decay coefficients in the horizontal and vertical spectra are different (Wu et al. 2018), with a more prominent peak always observed in the vertical velocity spectra than in the horizontal velocity spectra (Chen et al. 2018).

d. Objective of this study

The validation of the k^{-1} law in the velocity spectra is the subject of many studies, from laboratory to field experiments, but controversy remains. For example, Drobinski et al. (2004), Kunkel and Marusic (2006) and Ghannam et al. (2018) present clear evidence of the k^{-1} law for turbulence over land, but other studies (Wang and Zheng 2016; Mouri et al. 2019) have not. For turbulence over water surface, although the k^{-1} law is captured by Högström et al. (2002), Smedman et al. (2003) and Calaf et al. (2013), those observations were all above the WBL. Considering that the WBL is a layer where the interaction between ocean and atmosphere directly takes place and the fact that the logarithmic law or MOST is invalid there, distinct
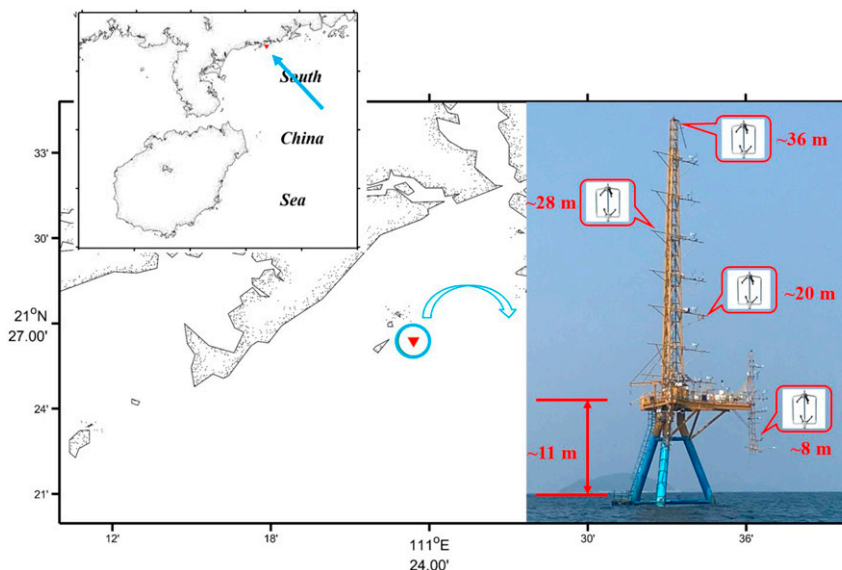
FIG. 1. The location and structure of the platform. The blue arrow points to the location of the platform.

properties may exist in the WBL. Therefore, the objective of this study is to explore the turbulent structure within or above the WBL by analyzing observational data obtained from a fixed platform before and during a cold front event when the ocean surface was dominated by swell and wind sea, respectively. We aimed to evaluate whether the turbulent characteristics in the marine ABL follow previous turbulent theories or models under different sea states.

This paper is organized as follows. The observational data are given in section 2, and the turbulent structure is analyzed in section 3. Section 4 presents a discussion, and a conclusion is provided in section 5.

2. Observation

a. Data description

The data used in this study are taken from a fixed platform in the South China Sea; the platform is ~6 km from the shore and is surrounded by water ~16 m deep (Fig. 1). During the measurements, several eddy-correlation systems, including ultrasonic anemometers and CO_2/H_2O analyzers, are mounted on the platform to record the three wind components and temperature. A seabed acoustic wave and current (AWAC) sensor (Nortek, Rud, Norway) is used to measure directional wave data.

Detailed information of the field experiment is given by Zou et al. (2017), Chen et al. (2018), and Zou et al. (2019), and thus, only the data used in this study are described here. The main instruments used in this study are four sets of Gill R3-50 ultrasonic anemometers and AWAC. The ultrasonic anemometers are mounted 8, 20, 28, and 36 m above the mean sea level to observe the turbulence at a frequency of 20 Hz. The AWAC observes waves every 3 h,

and each wave measurement lasts for 2048 s and has a sampling frequency of 1 Hz.

Figure 2 shows the time series of several variables before and during a cold front event. On 23 March 2012, cold air blew rapidly over the platform, leading to a quick drop of air temperature at 8 m from 26° to 18°C. At this time, the steady northeast wind speed reached approximately $18 \, \text{m s}^{-1}$, and the ocean surface was dominated by wind waves with wave ages (c_p/U_8, where c_p is the dominant peak wave speed, and U_8 is the wind speed at 8 m) less than 1. Compared with the strong wind during the cold front, the wind speed was not strong before the cold front, slowly decreasing from 7 to $1 \, \text{m s}^{-1}$; thus, the swell wave dominated the ocean surface ($c_p/U_8 > 1.2$). Figures 1 and 2b show that the swell wave propagated from the open sea without changing direction significantly, and the angle between the swell wave and wind direction was ~40°, suggesting wind-following swell.

In Fig. 2c, the atmospheric stability z/L computed at a height of 8 m is shown. Here, z is the height, $L = -(\overline{\theta_v} u_*^3)/(\kappa g \overline{u_3' \theta_v'})$ is the Obukhov length scale, κ is the von Kármán constant, g is the gravitational acceleration, θ_v is the virtual potential temperature, and $\overline{u_3' \theta_v'}$ is the flux of the virtual potential temperature. The slightly stable condition is predominant before the cold front; however, during the cold front, the stability changes from weakly stable to near neutral.

b. Data pretreatment

Unlike laboratory experiments, the environmental conditions during field observations are complex and uncontrollable. Thus, specific selection and strict quality control procedures are used to guarantee the accuracy of the results.

Studies (e.g., Grachev and Fairall 2001; Semedo et al. 2009; Chen et al. 2019) have shown that the depth of the WBL depends on the wave age, and the WBL height is typically only
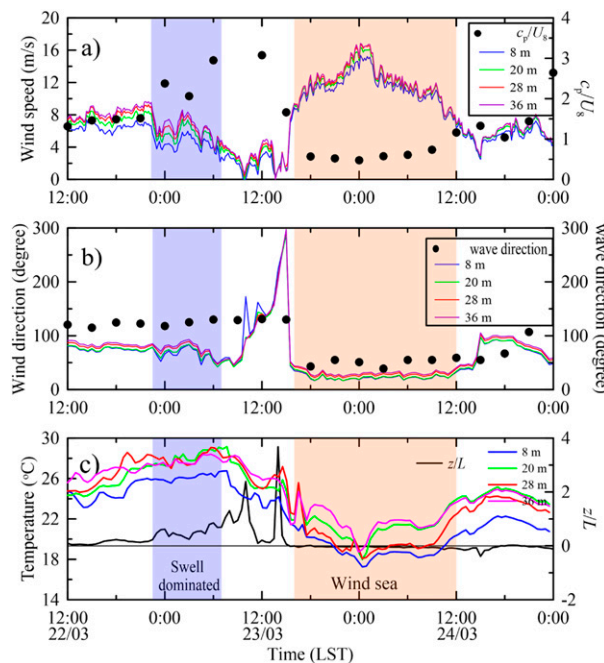
FIG. 2. Time series of (a) wind speed and nondimensional wave age, (b) wind direction and dominant wave direction ("from" direction), and (c) temperature and atmospheric stability at 8 m during and before a cold front. The orange shadow denotes the cold front, and the blue shadow denotes the swell-dominated region.

one or two wave heights for young wind waves [$O(1)$ m] but can extend to tens of meters or even the whole surface layer for old swell waves. Within the WBL, the wave-induced perturbations could exert a pronounced peak in the velocity spectrum (Rieder and Smith 1998; Soloviev and Kudryavtsev 2010; Högström et al. 2015). This peak is centered at the frequency of the dominant wave and can be a useful feature to check whether the observation is within the WBL.

During the cold front, data between 1600 LST 23 March and 1200 LST 24 March (the orange shadow in Fig. 2) are selected because the boundary layer is dominated by strong wind and the influence of the buoyancy is insignificant. At this time, as shown in section 3a, no peak is found in the velocity spectra at the frequency of the dominant wave; thus, all measurements are made outside the WBL.

Before the cold front, the boundary layer is slightly non-neutral. At this time, the shear driven turbulence could be affected by buoyancy force (Moeng and Sullivan 1994; Khanna and Brasseur 1998), which is inappropriately described by the AEM developed under neutral conditions. To avoid the buoyancy effect as much as possible, the time range of 2200 LST 22 March to 0700 LST 23 March is selected. During this time, the boundary was slightly stable ($z/L \approx 0.4$), and measurement at a height of 8 m was within the WBL because the wind speed was sufficiently small. Thus, swell could induce a pronounced peak in the wind velocity power spectrum (further shown in section 3a) (Högström et al. 2015; Högström et al. 2018; Zou et al. 2019).

Regarding the quality control, spike removal and mesoscale motion detection described by Zou et al. (2017) are used. The

spike removal discards the runs that contain more than 5% spikes, and mesoscale motion detection discards the runs that are affected by mesoscale motions. Tilt correction is used to correct the sonic anemometer tilt. Finally, the selected data are averaged every hour to obtain the mean wind speed and the turbulent fluctuations. After that, 16 runs during the cold front and 10 runs under swell condition are obtained.

Within the WBL, the Reynolds stress is the sum of the turbulence stress generated by shear and buoyancy forces and wave-coherent stress that accounts for the momentum transfer between the ocean waves and atmosphere (Hristov and Ruiz-Plancarte 2014). To remove the wave contribution from the total stress, the turbulent stress is derived following Zou et al. (2019).

c. Potential influence of coastline/swell waves

Figure 1 shows that when the offshore cold front blows from the northeast, the distance between the platform and the coastline is ~9 km. Compared with the open sea situations, the short fetch during the cold front may be associated with the internal boundary layer (IBL) due to the discontinuity of the surface properties between the ocean and land. Within IBL, Garratt (1990) shows that an inner layer appears near the surface, above which the wind profile shifts away from the logarithmic law. Fairall et al. (2006) and Mahrt et al. (2016) further show that the turbulence within IBL is suppressed and sea surface roughness is reduced when offshore wind of warm air blow over cooler water. Grachev et al. (2018) also describe a poor relationship between the nondimensional gradient of wind speed and the MOST. Geernaert (2002, 2010) proposes that the flux divergences present in an inhomogeneous region should be considered to extend MOST and obtain a more general form of the flux-profile relationship.

To analyze the influence of the IBL, the wind profiles during the cold front are first checked: a logarithmic velocity profile indicating the absence of IBL effect. In Fig. 3a, the normalized wind profiles U/u_* as a function of normalized height z/z_0 are plotted to check the potential influence of the coastline on the measurements. Here, the roughness length z_0 is determined by best fitting the wind profile that is above the WBL to the logarithmic law. The wind profile U as a function of height z is also given in inset figures for reference. Similarly, the wind profile before the cold front is also plotted in Fig. 3b to determine the potential influence of swell waves.

Figure 3a shows that during the cold front, the wind profiles almost collapse into a straight line, suggesting the full development of turbulence over the ocean surface, and the influence of the coastline can be neglected. Figure 3b shows that before the cold front, when the wind blows from the open sea and swells dominate, the wind profiles within the WBL always deviate from the logarithmic law, which is consistent with the results of Nilsson et al. (2012), Högström et al. (2013), etc. This is because the swell-induced upward momentum dominates near the surface to offset the upward momentum, and the wind gradient should become higher to generate more downward momentum. Above the WBL where the swell-exerted momentum decays to zero, the boundary layer is dominated only by shear and buoyancy-generated
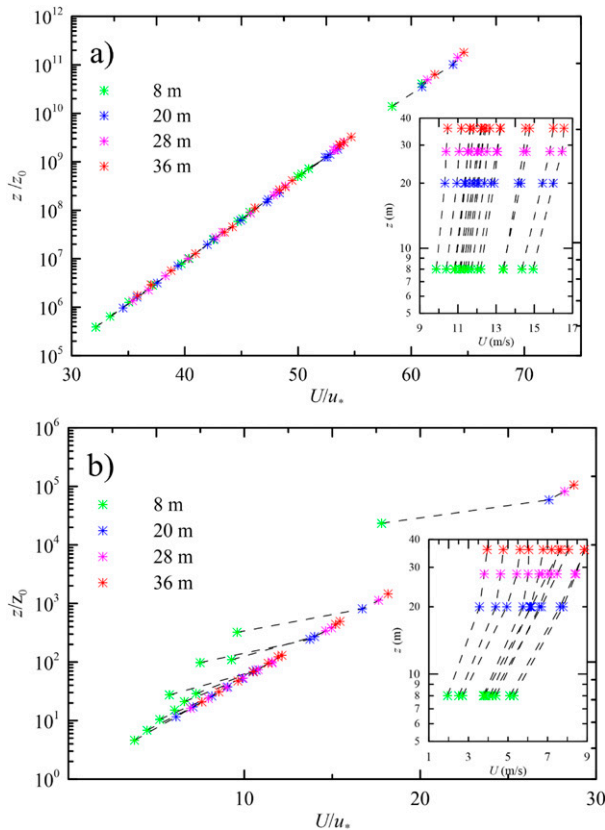
FIG. 3. Normalized wind profiles (U/u_*) as a function of normalized height (z/z_0) (a) during a cold front and (b) under swell conditions. The inset pictures show the wind profile as a function of height. The green, blue, magenta, and red asterisks represent the wind observed at 8, 20, 28, and 36 m, respectively. Each point was calculated by averaging over 1 h.

turbulence, so the logarithmic law appears again in the wind profile (Zou et al. 2020).

3. Results

a. Spectra

In Figs. 4 and 5, Fourier wind spectra, under cold front and swell conditions, versus wavenumber k are shown at a log–log scale. Considering the noise of the Fourier spectra, the spectra computed from Haar wavelet (Katul and Parlange 1994) are also added for comparison. Here, the premultiplied form of the spectra, kE_{ii}, is shown because the k^{-1} law would appear as a plateau in this form, which can be easily identified. Note that E_{ii} is the spatial spectra computed by converting the spectra in frequency space to wavenumber space using Taylor's frozen hypothesis (Taylor 1938). To address the influence of surface waves on the wind spectra, the wave spectra are plotted in the bottom panels of Figs. 4 and 5 after being converted to spatial spectra using the dispersion relation $\omega^2 = gk\tanh(kh)$, where $h = 16$ m is the water depth. We found that the spectrum shapes of all runs during the cold front are similar, so Figs. 4 and 5 only

show the result from one individual run each for brevity and the averaged spectra of all runs are given in the online supplemental material for reference.

The remarkable feature of the spectra is that there is a prominent inertial subrange (the $-2/3$ law in kE_{ii}) located in the high wavenumber range, under both cold front and swell conditions. According to the AEM, a k^{-1} law should appear in the longitudinal and lateral wind speed spectra in the intermediate range of spectra, and in this region, the k^{-1} range would be identified as a plateau (k^0) in kE_{ii}. In Fig. 4, both Fourier and wavelet spectra confirm that kE_{11} and kE_{22} exhibit plateaus that expand from one-third decade to almost one decade in wavenumber, and the length of plateaus in kE_{22} is longer than in kE_{11}.

Regarding the longitudinal premultiplied spectra, Guala et al. (2006), Horiguchi et al. (2010), and Vallikivi et al. (2015) report that two peaks can be identified at the beginning and end of the plateau: one at low wavenumbers associated with very large-scale motions (VLSMs; Kim and Adrian 1999; Guala et al. 2006) and another at high wavenumbers associated with large-scale motions (LSMs; Balakumar and Adrian 2007). During the cold front, the Fourier spectra (Fig. 4) show that several VLSM peaks appear at the end of the plateau of kE_{11}, where $k < \sim 10^{-2}$ m^{-1}. The VLSMs, especially those eddies ranging from 6×10^{-3} to 9×10^{-3} m^{-1} for kE_{11}, dampen with decreasing height, in agreement with a recent study at Qintu Lake in Minqin, China (Wang and Zheng 2016). The influence of VLSMs on the length of the plateau in the spectra is obvious. This makes the longitudinal plateau at 28 and 36 m narrower than those at 8 and 20 m. Combined with the VLSMs, the spectra at $8 \times 10^{-3} < k < \sim 2 \times 10^{-2}$ m^{-1} slightly deviate from k^0 with a steeper slope, which is consistent with Katul et al. (2012). For kE_{22}, similar features can also be found, except that VLSMs do not change with height.

Without the influence of VLSMs, Fig. 5 shows a long plateau in the intermediate wavenumber range of the longitudinal spectra under swell conditions. The lateral spectra under swell conditions are also much different from those during the cold front, with a swell-induced peak at a height of 8 m. The swell-induced peak has been reported by many studies, such as Soloviev and Kudryavtsev (2010), Högström et al. (2015), and Zou et al. (2019). Wu et al. (2018) show that the amplitude of the swell-induced spectra peak decays with increasing height; as a result, the swell-induced peak at the height of 20 m is too weak to be perceived, and plateaus appear again at heights of 28 and 36 m. Notably, the swell-induced spectra peak should have the same frequency as the swell waves. Figure 5 shows that the peak shifts away from that of the wave spectra for swell waves due to different dispersion relations when converting the frequency spectra to spatial spectra.

Equation (4) suggests that $kz \approx 1$ separates the regimes between the inertial subrange and intermediate range of the velocity spectra. This division is confirmed by the study of Drobinski et al. (2004). Note that several studies over land and lakes (e.g., Ghannam et al. 2018) suggest that kz should take 0.2–0.3. In Figs. 4 and 5, the vertical dashed lines at $kz = 1$ are added to the horizontal spectra. These dashed lines can adequately separate the two turbulent regimes in longitudinal spectra but not lateral spectra during the cold front. Under swell conditions, the plateau occurs at higher wavenumbers
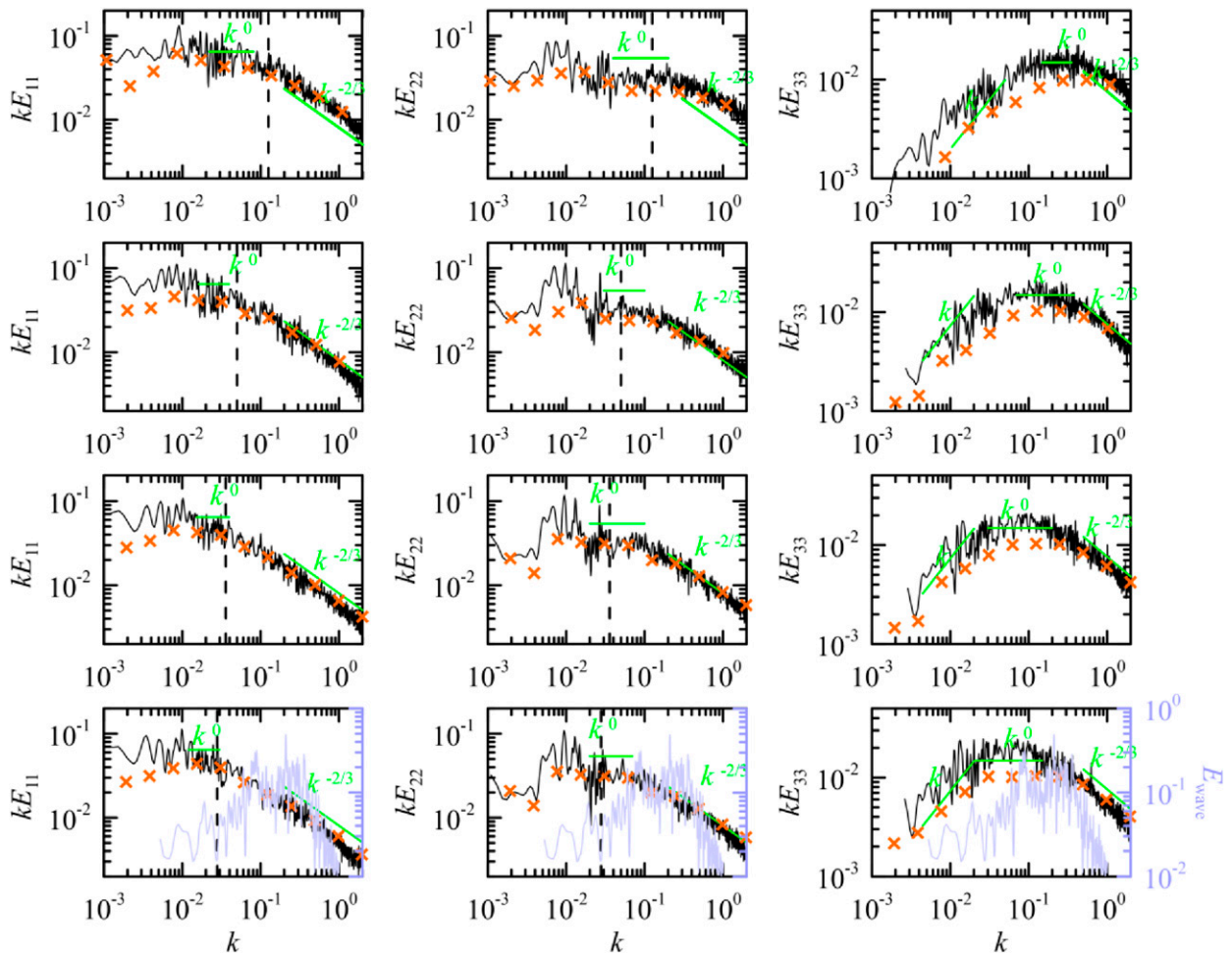
FIG. 4. Example of the spatial spectra changing with wavenumber under cold front conditions. The premultiplied form kE_{ii} is shown. The orange crosses are spectra computed from the Haar wavelet. The green lines marked with k, k^0, and $k^{-2/3}$ help determine slopes of the spectra subjectively. (bottom) The light blue lines are the wave spectra. The dashed vertical line in all panels shows $kz = 1$. (top)–(bottom) The spectra at 8, 20, 28, and 36 m.

than the dashed line. The shift of the break points to high wavenumbers is consistent with Smedman et al. (2003). Of note, for LSM, our data do not show a clear peak at the beginning of the plateau in Figs. 4 and 5.

Compared with the longitudinal and lateral velocity spectra, the vertical velocity spectra kE_{33} in Figs. 4 and 5 clearly exhibit a slope of k range at the low wavenumbers. The range between this low wavenumber and the inertial subrange determines the plateau. During the cold front, Fig. 4 shows that the length of the plateau in the vertical velocity spectra decreases with decreasing height due to the distortion of the ocean surface. Under swell conditions, similar to the lateral spectra, a remarkable swell-induced peak is found in the vertical velocity spectra at a height of 8 m, and plateaus occur above 20 m when the swell-induced peak decays to zero.

b. Cumulative stress distribution

Spectral analysis of VLSMs indicates that they have a significant effect on turbulent kinetic energy and Reynolds stress

(Guala et al. 2006; Balakumar and Adrian 2007; Barthlott et al. 2007), which distinguishes them from the inactive motions proposed by Townsend (1976). For example, Balakumar and Adrian (2007) report that more than 40% of the Reynolds stress is due to the existence of VLSMs in channel and zero-pressure-gradient boundary layer flows and ~50% in pipe flows. To determine how much those VLSMs contribute to the wind total stress, the cases shown in Figs. 4 and 5 are used to compute the cumulative stress distribution:

$$\gamma_{iw}(k) = -\int_{k_{\max}}^{k} E_{iw}(\tilde{k}) \frac{d\tilde{k}}{u_*^2}, \quad i = 1, 2, \tag{5}$$

where E_{iw} is the cospectra and $k_{\max}$ represents the maximum wavenumber in E_{iw}; γ_{iw} represents the cumulative contribution of all the wavenumbers from $k_{\max}$ to k, while $1 - \gamma_{iw}$ represents the contribution from all wavenumbers less than k.

Figures 6 and 7 present the cumulative Reynolds stress fraction as a function of the wavenumber. The vertical lines
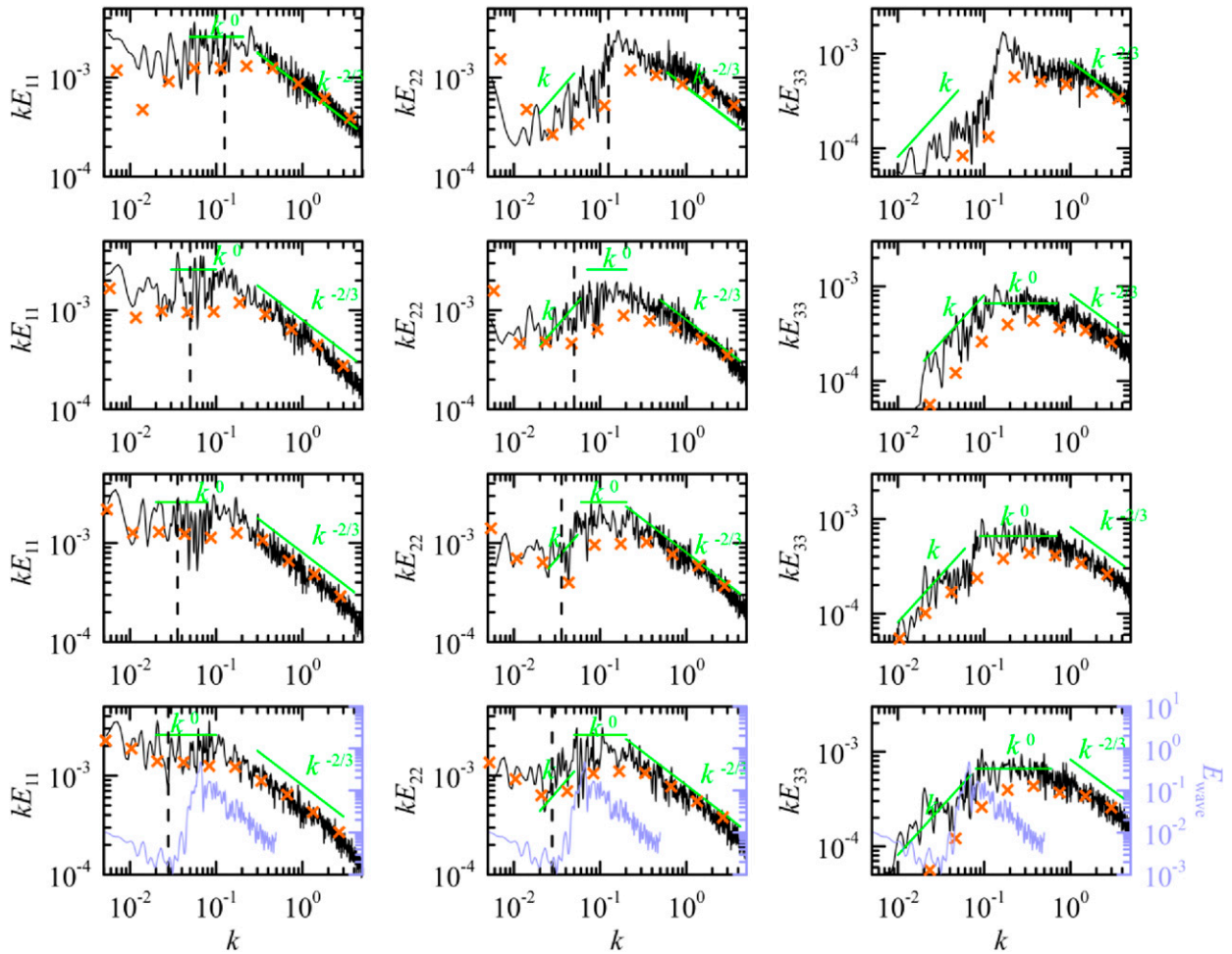
FIG. 5. As in Fig. 4, but for the swell condition.

with arrowheads in Fig. 6 show the beginning of VLSMs. The result shows that the VLSMs carry most of the Reynolds stress under cold front conditions, ranging from 30% to 50%. This range is consistent with the results of Drobinski et al. (2004) and Barthlott et al. (2007). From the experiments in turbulent pipes, wind channels and zero-pressure-gradient boundary layers, Guala et al. (2006) and Balakumar and Adrian (2007) report that the contribution of VLSMs to the wind total stress increases with increasing height. In the marine surface layer, our data also show this phenomenon (Fig. 6).

The influence of a swell on wind stress has been recently studied by Zou et al. (2019). They find that the measurements within the WBL accurately record the swell-induced perturbation, which can be observed in the cumulative stress distribution (also called the Ogive curve). In Fig. 7, the longitudinal cumulative stress distribution at a height of 8 m becomes flat, while the lateral cumulative stress distribution increases abruptly with decreasing wavenumber in the swell-affected region. However, at other heights, no obvious influence of the swell wave is found. According to the analysis of Zou et al. (2019), this difference is because the wave-induced perturbation decays quickly with increasing height; thus, the

wave-coherent stress accounts for only a small portion of the wind total stress.

c. Velocity variances

In this section, the velocity variances are used to test the universality of Eqs. (1)–(3). By integrating the spatial spectra from the end of the k^{-1} range to k_{max}, the velocity variances, which are normalized by u_*^2, are shown in Fig. 8 as a function of height. For the measurement within the WBL, the turbulent stress is used to normalize the velocity variances to eliminate any influence of the swell wave on the wind stress.

Figure 8a shows that under cold front conditions, the normalized longitudinal and lateral velocity variances first increase with increasing height, reaching a maximum at a height of 20 m, then decrease with increasing height. This result is roughly consistent with the land observation and LES results by Drobinski et al. (2004, 2007). Above 20 m, the mean velocity variances follow Eq. (1) (the dashed lines in Fig. 8a), demonstrating the logarithmic scaling of variance with height over the ocean surface.

The vertical velocity variance in the surface layer is usually considered to be constant with height [Eq. (2)]. However, the
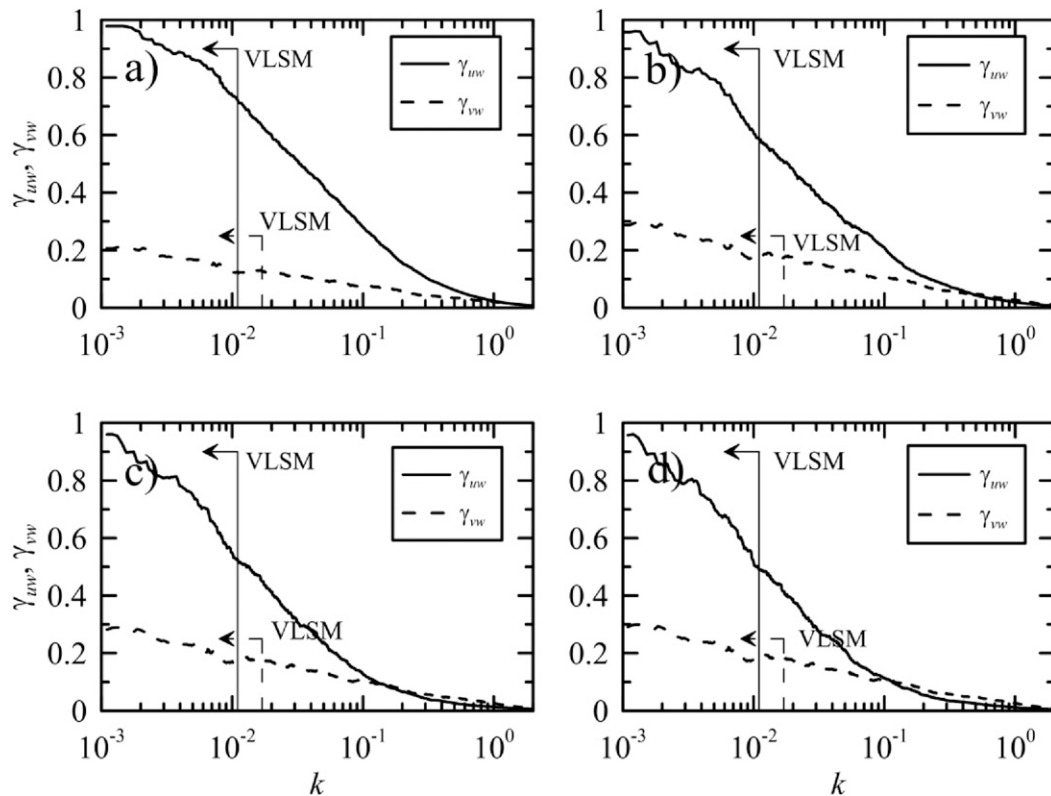
FIG. 6. Cold-frontal cumulative stress distribution as a function of wavenumber at (a) 8, (b) 20, (c) 28, and (d) 36 m. The vertical lines with arrowheads show the VLSMs.

''top-down'' model predicts that the vertical velocity variance within the surface layer should increase with a power law of 2/3. This is further demonstrated by Drobinski et al. (2004) in the ESL. To determine whether our result also follows the ''top-down'' model, the best fit line (solid black line) with Eq. (3) using the least squares method is plotted in Fig. 8a. This figure shows that our data follow Eq. (3) within the surface layer.

Under swell conditions, the behavior of velocity variances shows a remarkable difference from that under cold front conditions (Fig. 8b). The magnitudes of the velocity variances under swell conditions are much larger than those during the cold front, and all velocity variances first decrease and then increase with increasing height. This result is not consistent with Eqs. (1)–(3) but is similar to the results of recent studies via LES (Sullivan et al. 2008), especially for vertical velocity variances.

d. Quadrant analysis of the momentum flux

Following Lin et al. (1996) and Smedman et al. (1999), the total momentum flux can be divided into four quadrants according to the signs of u' and w': 1) $u' \geq 0$, $w' \geq 0$ (outward interaction); 2) $u' < 0$, $w' \geq 0$ (ejection); 3) $u' < 0$, $w' < 0$ (inward interaction); and 4) $u' \geq 0$, $w' < 0$ (sweep).

In conditions where wind blows over land surface, both observations (Drobinski et al. 2004; Horiguchi et al. 2010;

Horiguchi et al. 2012) and LES modeling results (Lin et al. 1996; Drobinski et al. 2007) have shown that the momentum flux is dominated by ejection and sweep because they contribute mostly to the transfer of momentum downward, while inward and outward momentum transfers are less frequent and weaker in magnitude. The cold front result in Fig. 9a is consistent with earlier studies (e.g., Drobinski et al. 2004; Drobinski et al. 2007), with a ratio of ~0.24 between the positive flux fraction and the negative flux fraction. However, under swell conditions, the ratio increases to ~0.55, which is consistent with the result of coupled boundary layer air–sea transfer (Sullivan et al. 2008).

Drobinski et al. (2004) and Horiguchi et al. (2012) show that in the SSL, the flux fraction due to the ejection motion is slightly higher than that due to the sweep motion, but in the ESL, ejections and sweeps contribute equally to the momentum flux. Furthermore, Horiguchi et al. (2010, 2012) reveal that large-scale motions cause sweep motion to contribute more than ejection motion to the flux, in agreement with the study by Lin et al. (1996). However, our data do not show such a phenomenon (Fig. 9a). The smaller difference between ejection and sweep motions at a height of 8 m suggests that our result is similar to that of Drobinski et al. (2004).

Under swell conditions, the momentum flux profile is much different from that during the cold front. The flux fraction due to ejection (inward) motion is almost equal to that due to the
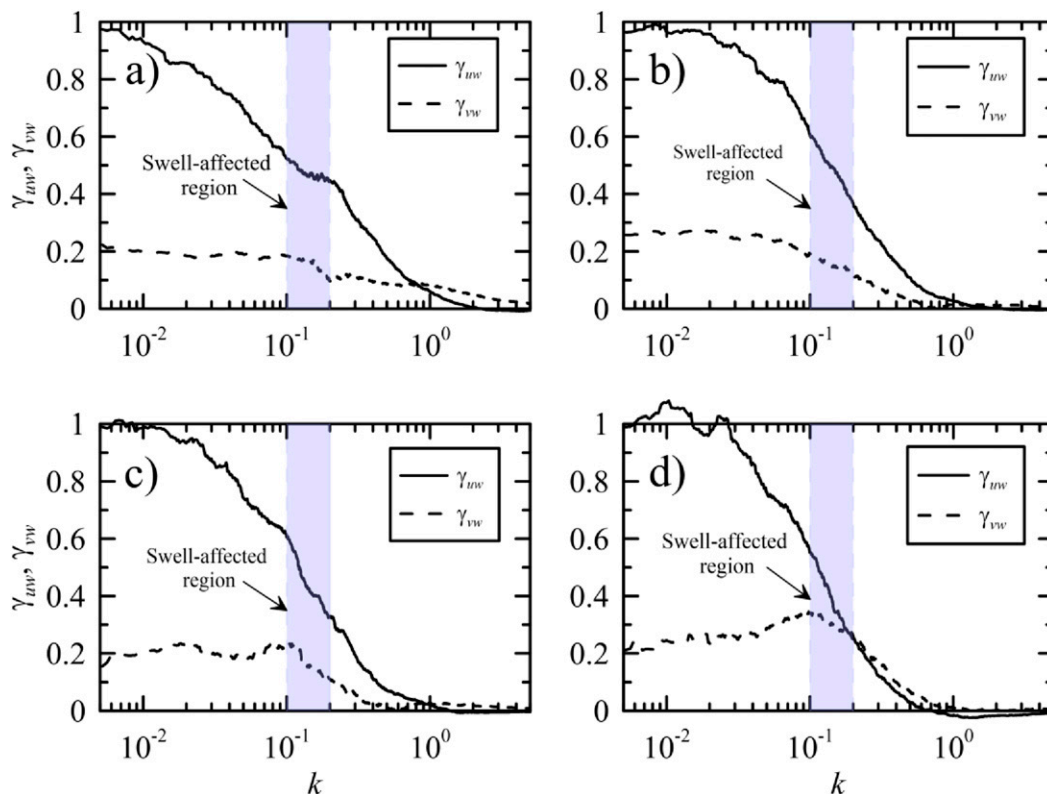
FIG. 7. As in Fig. 6, but for the swell condition.

sweep (outward) motion. The magnitudes of the four fractions increase with increasing height above the WBL, but decrease with increasing height within the WBL.

4. Discussion

To relate the Reynolds stress transferred across the air–sea interface, the logarithmic wind profile based on Prandtl mixing-length theory is widely used in oceanic and atmospheric models. The assumption of a logarithmic wind profile is also used in parameterization of ocean surface roughness and converting the observation to standard height—i.e., 10 m above the sea surface. However, recent observations (e.g., Smedman et al. 2009; Högström et al. 2013; Babanin et al. 2018; Voermans et al. 2019) have suggested that the logarithmic wind profile is invalid within the WBL. According to AEM, the k^{-1} law represents the other side of the logarithmic law. Thus, comparing the turbulence structure over the ocean surface with that close to the wall or over land can help us understand why the logarithmic wind profile is invalid within the WBL.

a. Wind-sea conditions

Our results indicate that the velocity spectra during the cold front have a k^{-1} law in the intermediate range of the wavenumber. For velocity variances, Fig. 8a shows that they follow Eqs. (1) and (3), which is consistent with the theoretical studies based on laboratory and field experiments. These features

indicate that the turbulence over the wind sea surface is similar to that over a flat land surface.

Earlier laboratory experiments (e.g., Zhao and Smits 2007; Hultmark et al. 2013; Vallikivi et al. 2015) have revealed that the horizontal velocity variances display two maxima. The first maximum is located near the surface, where viscosity is important, and corresponds to the point where the production of turbulent kinetic energy is highest. The second maximum appears far from the surface and exists only under very high Reynolds number, representing the continued influence of viscosity. The maximum identified in Fig. 8a corresponds to the second maximum in the ABL, because the first maximum appears only near the surface, corresponding to a height of 5 mm in the ABL, which is out of the range of our observations.

Laboratory experiments have also suggested that the second maximum is the lower limit height of the logarithmic velocity variances. Our data show that above this maximum, the mean velocity variances follow Eq. (1).

The maximum velocity variance provides an effective index to check the validation of the turbulent closure scheme in the Reynolds-averaged Navier–Stokes equations. According to Hultmark et al. (2013) and Marušić et al. (2013), the second maximum in the variance profile is observed in the logarithmic wind profile region where the production and dissipation of turbulence should be in equilibrium. However, the appearance of the second maximum implies that equilibrium does not exist because the wind gradient decreases monotonically with increasing height. This disequilibrium between turbulent
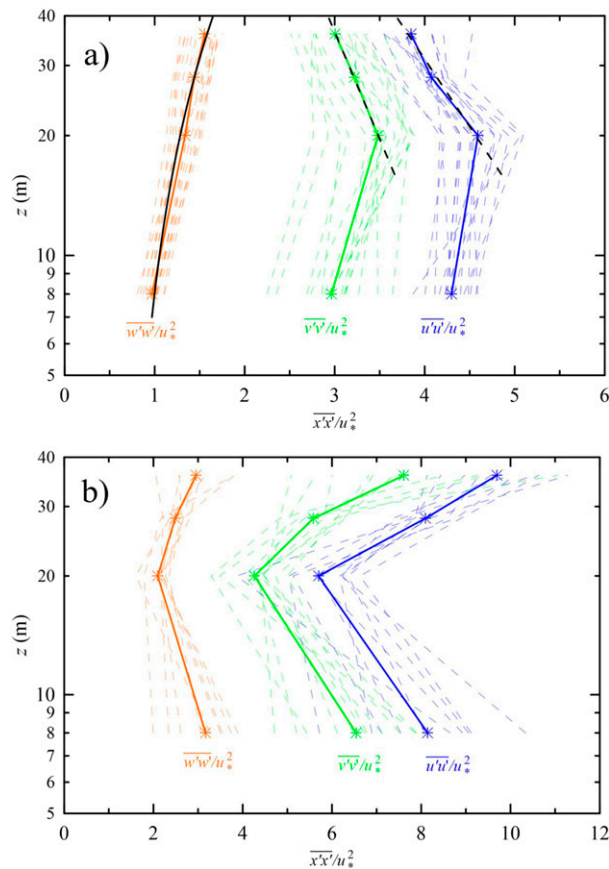
FIG. 8. Vertical profiles of nondimensional variance components (a) during a cold front and (b) under swell conditions. The variance components were calculated from turbulence after removing the mean wind speed. The averaged time of 1 h was used to obtain the mean wind speed. The blue, green, and orange lines represent the longitudinal, lateral, and vertical velocity variances, respectively. The thin dashed lines are all the data used in this study, and the solid lines represent averaged values. The black dashed and solid lines in (a) are the best fit to Eqs. (2) and (3), respectively.
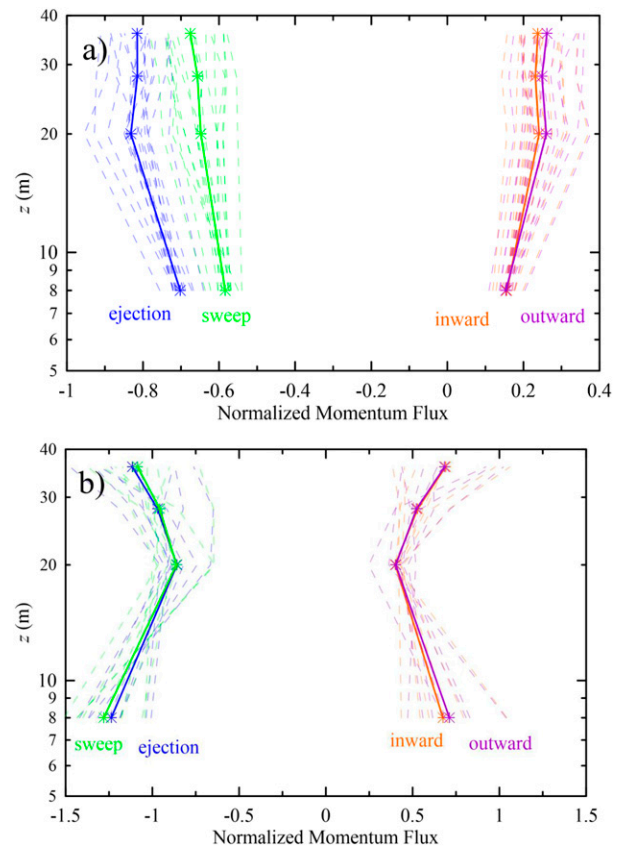
FIG. 9. Vertical profiles of normalized momentum fluxes (a) during a cold front and (b) under swell conditions. The momentum fluxes were calculated from turbulence after removing the mean wind speed. The averaged time of 1 h was used to obtain the mean wind speed. The data within the WBL are normalized by turbulent stress, and others use total stress. The blue, green, orange, and purple lines represent ejection, sweep, and inward and outward motions, respectively. The thin dashed lines are all the data used in this study, and the solid lines represent averaged values.

production and dissipation is also reported by Ghannam et al. (2018) in both field and laboratory experiments. Considering the presence of two overlapping regions in the wind profile (McKeon et al. 2004), the formation of the second maximum may be due to the different overlap above and below the maximum. It is suggested that the second maximum in the horizontal velocity variance should be considered to improve the accuracy of the turbulent closure model.

b. Swell condition

Figure 5 shows that near the surface, a swell-related peak dominates in the velocity spectra. The pronounced swell-related peak suggests that the wave-coherent perturbations other than the attached eddies dominated in the WBL. This is why the wind within the WBL deviates from the logarithmic law. According to Sullivan et al. (2008), the upward momentum exerted by swell appears as outward and inward motions. As a result, the outward and inward flux within the WBL will

increase with decreasing height (Fig. 9b). The wind profiles within the WBL have a great gradient (Fig. 3b), so the velocity variances and the magnitude of sweep and ejection motions at a height of 8 m are larger than those at 20 m.

Because the wave-coherent perturbations are constrained within the WBL, a remarkably long k^{-1} region appears in the velocity spectra above the WBL. As mentioned in the introduction section, the k^{-1} range and logarithmic law of velocity variances are equivalent. However, it is interesting that the velocity variances (Fig. 8b) do not follow Eqs. (1)–(3). Additionally, the normalized momentum flux above 20 m in Fig. 9b also has distinct features compared to cold front conditions.

The first reason considered to explain the above feature is the buoyancy effect. Li et al. (2018) recently implied that the outer-scaled turbulent motion can be enhanced by buoyancy force to cause nondimensional wind profile to deviate from MOST. Thus, in addition to the attached

eddies, the outer-scaled eddies play a decisive role in the surface layer, suggesting a possible effect of the "top-down" mechanism proposed by Hunt and Morrison (2000). However, the outer-scaled eddies cannot fully explain our result because before the cold front, the boundary layer is slightly stable, so no updraft/subsidence, as mentioned by Li et al. (2018), appears in the boundary layer.

Considering the different terrains between our measurement and earlier studies, another possible reason may be the existence of swell waves. However, Fig. 5 shows that the effect of swell waves is constrained within the WBL and thus has nothing to do with the turbulence above 20 m.

Therefore, further studies, especially based on observations or new theory, are still required to address this issue.

5. Conclusions

In this study, the turbulent structure within the marine ABL is investigated by using four levels of measurement at a fixed platform in the South China Sea. The data during and before a cold front were selected to study the behavior of the wind spectra, cumulative stress distribution, velocity variance and momentum distribution under these two different sea state conditions.

The main results of this study are as follows:

- During the cold front, when the ocean surface is dominated by wind waves, a logarithmic height dependence of the wind profile is observed. However, before the cold front, the wind profile shows a clear deviation from the logarithmic height dependence due to the existence of a wind-following swell.
- A k^{-1} law is observed in the intermediate range of the velocity spectra, during both cold front and swell conditions, confirming the validation of the attached eddy hypothesis over ocean surfaces.
- VLSMs carry a large proportion of the total Reynolds stress (Fig. 6). The effect of swell on the Reynolds stress is remarkable in the cumulative stress distribution (Fig. 7).
- The horizontal velocity variances during the cold front have a maximum at a height of 20 m, and the maximum signals the beginning of the logarithmic height dependence of the velocity variances. The vertical velocity variance increases with increasing height following a power law of 2/3 other than a constant.
- Before the cold front event when swell dominants, the vertical profile velocity variances and momentum flux first decrease and then increase with increasing height (Figs. 8b and 9b) and are different from those under wind-sea conditions.

REFERENCES

Babanin, A. V., J. McConochie, and D. Chalikov, 2018: Winds near the surface of waves: Observations and modeling. *J. Phys. Oceanogr.*, **48**, 1079–1088, https://doi.org/10.1175/JPO-D-17-0009.1.

Balakumar, B. J., and R. J. Adrian, 2007: Large- and very-large-scale motions in channel and boundary-layer flows. *Philos. Trans. Roy. Soc.*, **365A**, 665–681, https://doi.org/10.1098/rsta.2006.1940.

Barthlott, C., P. Drobinski, C. Fesquet, T. Dubos, and C. Pietras, 2007: Long-term study of coherent structures in the atmospheric surface layer. *Bound.-Layer Meteor.*, **125**, 1–24, https://doi.org/10.1007/s10546-007-9190-9.

Buckley, M. P., and F. Veron, 2016: Structure of the airflow above surface waves. *J. Phys. Oceanogr.*, **46**, 1377–1397, https://doi.org/10.1175/JPO-D-15-0135.1.

Calaf, M., M. Hultmark, H. J. Oldroyd, V. Simeonov, and M. B. Parlange, 2013: Coherent structures and the k^{-1} spectral behaviour. *Phys. Fluids*, **25**, 125107, https://doi.org/10.1063/1.4834436.

Chamecki, M., N. L. Dias, S. T. Salesky, and Y. Pan, 2017: Scaling laws for the longitudinal structure function in the atmospheric surface layer. *J. Atmos. Sci.*, **74**, 1127–1147, https://doi.org/10.1175/JAS-D-16-0228.1.

Chen, S., F. Qiao, C. J. Huang, and B. Zhao, 2018: Deviation of wind stress from wind direction under low wind conditions. *J. Geophys. Res. Oceans*, **123**, 9357–9368, https://doi.org/10.1029/2018JC014137.

——, ——, W. Jiang, J. Guo, and D. Dai, 2019: Impact of surface waves on wind stress under low to moderate wind conditions. *J. Phys. Oceanogr.*, **49**, 2017–2028, https://doi.org/10.1175/JPO-D-18-0266.1.

Drobinski, P., P. Carlotti, R. K. Newsom, R. M. Banta, R. C. Foster, and J.-L. Redelsperger, 2004: The structure of the near-neutral atmospheric surface layer. *J. Atmos. Sci.*, **61**, 699–714, https://doi.org/10.1175/1520-0469(2004)061<0699:TSOTNA>2.0.CO;2.

——, ——, J.-L. Redelsperger, V. Masson, R. M. Banta, and R. K. Newsom, 2007: Numerical and experimental investigation of the neutral atmospheric surface layer. *J. Atmos. Sci.*, **64**, 137–156, https://doi.org/10.1175/JAS3831.1.

Fairall, C. W., and Coauthors, 2006: Turbulent bulk transfer coefficients and ozone deposition velocity in the international consortium for atmospheric research into transport and transformation. *J. Geophys. Res.*, **111**, D23S20, https://doi.org/10.1029/2006JD007597.

Garratt, J. R., 1990: The internal boundary layer—A review. *Bound.-Layer Meteor.*, **50**, 171–203, https://doi.org/10.1007/BF00120524.

Geernaert, G. L., 2002: On extending the flux-profile similarity theory to include quasi-homogeneous conditions in the marine atmospheric surface layer. *Bound.-Layer Meteor.*, **105**, 433–450, https://doi.org/10.1023/A:1020307703242.

——, 2010: Normalizing air–sea flux coefficients for horizontal homogeneity, stationarity, and neutral stratification. *J. Phys. Oceanogr.*, **40**, 2148–2158, https://doi.org/10.1175/2010JPO4407.1.

Ghannam, K., G. G. Katul, E. Bou-Zeid, T. Gerken, and M. Chamecki, 2018: Scaling and similarity of the anisotropic coherent eddies in near-surface atmospheric turbulence. *J. Atmos. Sci.*, **75**, 943–964, https://doi.org/10.1175/JAS-D-17-0246.1.

Grachev, A. A., and C. W. Fairall, 2001: Upward momentum transfer in the marine boundary layer. *J. Phys. Oceanogr.*, **31**,

1698–1711, https://doi.org/10.1175/1520-0485(2001)031<1698:UMTITM>2.0.CO;2.

——, ——, J. E. Hare, J. B. Edson, and S. D. Miller, 2003: Wind stress vector over ocean waves. *J. Phys. Oceanogr.*, **33**, 2408–2429, https://doi.org/10.1175/1520-0485(2003)033<2408:WSVOOW>2.0.CO;2.

——, L. S. Leo, H. J. S. Fernando, C. W. Fairall, E. Creegan, B. W. Blomquist, A. J. Christman, and C. M. Hocut, 2018: Air–sea/land interaction in the coastal zone. *Bound.-Layer Meteor.*, **167**, 181–210, https://doi.org/10.1007/s10546-017-0326-2.

Guala, M., S. E. Hommema, and R. J. Adrian, 2006: Large-scale and very-large-scale motions in turbulent pipe flow. *J. Fluid Mech.*, **554**, 521–542, https://doi.org/10.1017/S0022112006008871.

Högström, U., J. C. R. Hunt, and A.-S. Smedman, 2002: Theory and measurements for turbulence spectra and variances in the atmospheric neutral surface layer. *Bound.-Layer Meteor.*, **103**, 101–124, https://doi.org/10.1023/A:1014579828712.

——, A. Smedman, E. Sahleé, W. M. Drennan, K. K. Kahma, H. Pettersson, and F. Zhang, 2009: The atmospheric boundary layer during swell: A field study and interpretation of the turbulent kinetic energy budget for high wave ages. *J. Atmos. Sci.*, **66**, 2764–2779, https://doi.org/10.1175/2009JAS2973.1.

——, A. Rutgersson, E. Sahlée, A.-S. Smedman, T. S. Hristov, W. M. Drennan, and K. K. Kahma, 2013: Air–sea interaction features in the Baltic Sea and at a Pacific trade-wind site: An inter-comparison study. *Bound.-Layer Meteor.*, **147**, 139–163, https://doi.org/10.1007/s10546-012-9776-8.

——, E. Sahlée, A.-S. Smedman, A. Rutgersson, E. Nilsson, K. K. Kahma, and W. M. Drennan, 2015: Surface stress over the ocean in swell-dominated conditions during moderate winds. *J. Atmos. Sci.*, **72**, 4777–4795, https://doi.org/10.1175/JAS-D-15-0139.1.

——, ——, ——, ——, ——, ——, and ——, 2018: The transition from downward to upward air–sea momentum flux in swell-dominated light wind conditions. *J. Atmos. Sci.*, **75**, 2579–2588, https://doi.org/10.1175/JAS-D-17-0334.1.

Horiguchi, M., T. Hayashi, H. Hashiguchi, Y. Ito, and H. Ueda, 2010: Observations of coherent turbulence structures in the near-neutral atmospheric boundary layer. *Bound.-Layer Meteor.*, **136**, 25–44, https://doi.org/10.1007/s10546-010-9500-5.

——, ——, A. Adachi, and S. Onogi, 2012: Large-scale turbulence structures and their contributions to the momentum flux and turbulence in the near-neutral atmospheric boundary layer observed from a 213-m tall meteorological tower. *Bound.-Layer Meteor.*, **144**, 179–198, https://doi.org/10.1007/s10546-012-9718-5.

Hristov, T., and J. Ruiz-Plancarte, 2014: Dynamic balances in a wavy boundary layer. *J. Phys. Oceanogr.*, **44**, 3185–3194, https://doi.org/10.1175/JPO-D-13-0209.1.

Hultmark, M., M. Vallikivi, S. C. C. Bailey, and A. J. Smits, 2013: Logarithmic scaling of turbulence in smooth- and rough-wall pipe flow. *J. Fluid Mech.*, **728**, 376–395, https://doi.org/10.1017/jfm.2013.255.

Hunt, J. C. R., and J. F. Morrison, 2000: Eddy structure in turbulent boundary layers. *Eur. J. Mech.*, **19**, 673–694, https://doi.org/10.1016/S0997-7546(00)00129-1.

——, and P. Carlotti, 2001: Statistical structure at the wall of the high Reynolds number turbulent boundary layer. *Flow Turbul. Combust.*, **66**, 453–475, https://doi.org/10.1023/A:1013519021030.

Hutchins, N., K. Chauhan, I. Marusic, J. Monty, and J. Klewicki, 2012: Towards reconciling the large-scale structure of turbulent boundary layers in the atmosphere and laboratory. *Bound.-Layer Meteor.*, **145**, 273–306, https://doi.org/10.1007/s10546-012-9735-4.

Jiang, Q., P. Sullivan, S. Wang, J. Doyle, and L. Vincent, 2016: Impact of swell on air–sea momentum flux and marine boundary layer under low-wind conditions. *J. Atmos. Sci.*, **73**, 2683–2697, https://doi.org/10.1175/JAS-D-15-0200.1.

Katul, G. G., and M. B. Parlange, 1994: On the active role of temperature in surface-layer turbulence. *J. Atmos. Sci.*, **51**, 2181–2195, https://doi.org/10.1175/1520-0469(1994)051<2181:OTAROT>2.0.CO;2.

——, A. Porporato, and V. Nikora, 2012: Existence of k^{-1} power-law scaling in the equilibrium regions of wall-bounded turbulence explained by Heisenberg's eddy viscosity. *Phys. Rev. E*, **86**, 066311, https://doi.org/10.1103/PhysRevE.86.066311.

Khanna, S., and J. G. Brasseur, 1998: Three-dimensional buoyancy- and shear-induced local structure of the atmospheric boundary layer. *J. Atmos. Sci.*, **55**, 710–743, https://doi.org/10.1175/1520-0469(1998)055<0710:TDBASI>2.0.CO;2.

Kim, K. C., and R. J. Adrian, 1999: Very large-scale motion in the outer layer. *Phys. Fluids*, **11**, 417–422, https://doi.org/10.1063/1.869889.

Kunkel, G. J., and I. Marusic, 2006: Study of the near-wall-turbulent region of the high-Reynolds-number boundary layer using an atmospheric flow. *J. Fluid Mech.*, **548**, 375–402, https://doi.org/10.1017/S0022112005007780.

Li, Q., P. Gentine, J. P. Mellado, and K. A. McColl, 2018: Implications of nonlocal transport and conditionally averaged statistics on Monin–Obukhov similarity theory and Townsend's attached eddy hypothesis. *J. Atmos. Sci.*, **75**, 3403–3431, https://doi.org/10.1175/JAS-D-17-0301.1.

Lin, C. L., J. C. McWilliams, C. H. Moeng, and P. P. Sullivan, 1996: Coherent structures and dynamics in a neutrally stratified planetary boundary layer flow. *Phys. Fluids*, **8**, 2626–2639, https://doi.org/10.1063/1.869048.

Mahrt, L., E. L. Andreas, J. B. Edson, D. Vickers, J. Sun, and E. G. Patton, 2016: Coastal zone surface stress with stable stratification. *J. Phys. Oceanogr.*, **46**, 95–105, https://doi.org/10.1175/JPO-D-15-0116.1.

Marušić, I., and A. E. Perry, 1995: A wall-wake model for the turbulence structure of boundary layers. Part II. Further experimental support. *J. Fluid Mech.*, **298**, 389–407, https://doi.org/10.1017/S0022112095003363.

——, J. P. Monty, M. Hultmark, and A. J. Smits, 2013: On the logarithmic region in wall turbulence. *J. Fluid Mech.*, **716**, R3, https://doi.org/10.1017/jfm.2012.511.

McKeon, B. J., J. Li, W. Jiang, J. F. Morrison, and A. J. Smits, 2004: Further observations on the mean velocity distribution in fully developed pipe flow. *J. Fluid Mech.*, **501**, 135–147, https://doi.org/10.1017/S0022112003007304.

Mei, A., and T. L. Bo, 2019: Spatial variation of statistical and spectral properties of the stream wise and wall-normal velocity fluctuations in the near-neutral atmospheric surface layer. *Bound.-Layer Meteor.*, **173**, 223–242, https://doi.org/10.1007/s10546-019-00465-0.

Moeng, C.-H., and P. P. Sullivan, 1994: A comparison of shear- and buoyancy-driven planetary boundary layer flows. *J. Atmos. Sci.*, **51**, 999–1022, https://doi.org/10.1175/1520-0469(1994)051<0999:ACOSAB>2.0.CO;2.

Mouri, H., T. Morinaga, and S. Haginoya, 2019: Unlikely existence of k_x^{-1} spectral law in wall turbulence: An observation of the

atmospheric surface layer. *Phys. Fluids*, **31**, 035103, https://doi.org/10.1063/1.5063545.

Nilsson, E. O., A. Rutgersson, A.-S. Smedman, and P. P. Sullivan, 2012: Convective boundary-layer structure in the presence of wind-following swell. *Quart. J. Roy. Meteor. Soc.*, **138**, 1476–1489, https://doi.org/10.1002/qj.1898.

Pan, Y., and M. Chamecki, 2016: A scaling law for the shear-production range of second-order structure functions. *J. Fluid Mech.*, **801**, 459–474, https://doi.org/10.1017/jfm.2016.427.

Perry, A. E., and M. S. Chong, 1982: On the mechanism of wall turbulence. *J. Fluid Mech.*, **119**, 173–217, https://doi.org/10.1017/S0022112082001311.

——, and I. Marušić, 1995: A wall-wake model for the turbulence structure of boundary layers. Part I. Extension of the attached eddy hypothesis. *J. Fluid Mech.*, **298**, 361–388, https://doi.org/10.1017/S0022112095003351.

——, S. Henbest, and M. S. Chong, 1986: A theoretical and experimental study of wall turbulence. *J. Fluid Mech.*, **165**, 163–199, https://doi.org/10.1017/S002211208600304X.

Rieder, K. F., and J. A. Smith, 1998: Removing wave effects from the wind stress vector. *J. Geophys. Res.*, **103**, 1363–1374, https://doi.org/10.1029/97JC02571.

Semedo, A., Ø. Saetra, A. Rutgersson, K. K. Kahma, and H. Pettersson, 2009: Wave-induced wind in the marine boundary layer. *J. Atmos. Sci.*, **66**, 2256–2271, https://doi.org/10.1175/2009JAS3018.1.

Smedman, A., U. Högström, H. Bergström, A. Rutgersson, K. K. Kahma, and H. Pettersson, 1999: A case study of air-sea interaction during swell conditions. *J. Geophys. Res.*, **104**, 25 833–25 851, https://doi.org/10.1029/1999JC900213.

——, ——, and A. Sjöblom, 2003: A note on velocity spectra in the marine boundary layer. *Bound.-Layer Meteor.*, **109**, 27–48, https://doi.org/10.1023/A:1025428024311.

——, ——, E. Sahleé, W. M. Drennan, K. K. Kahma, H. Pettersson, and F. Zhang, 2009: Observational study of marine atmospheric boundary layer characteristics during swell. *J. Atmos. Sci.*, **66**, 2747–2763, https://doi.org/10.1175/2009JAS2952.1.

Soloviev, Y. P., and V. N. Kudryavtsev, 2010: Wind-speed undulations over swell: Field experiment and interpretation. *Bound.-Layer Meteor.*, **136**, 341–363, https://doi.org/10.1007/s10546-010-9506-z.

Sullivan, P. P., J. B. Edson, T. Hristov, and J. C. McWilliams, 2008: Large-eddy simulations and observations of atmospheric marine boundary layers above nonequilibrium surface waves. *J. Atmos. Sci.*, **65**, 1225–1245, https://doi.org/10.1175/2007JAS2427.1.

Sun, J., and J. R. French, 2016: Air–sea interactions in light of new understanding of air–land interactions. *J. Atmos. Sci.*, **73**, 3931–3949, https://doi.org/10.1175/JAS-D-15-0354.1.

Taylor, G. I., 1938: The spectrum of turbulence. *Proc. Roy. Soc. London*, **164A**, 476–490, https://doi.org/10.1098/rspa.1938.0032.

Townsend, A. A., 1976: *The Structure of Turbulent Shear Flow*. Cambridge University Press, 429 pp.

Vallikivi, M., B. Ganapathisubramani, and A. J. Smits, 2015: Spectral scaling in boundary layers and pipes at very high Reynolds numbers. *J. Fluid Mech.*, **771**, 303–326, https://doi.org/10.1017/jfm.2015.181.

Voermans, J. J., H. Rapizo, H. Ma, F. Qiao, and A. V. Babanin, 2019: Air–sea momentum fluxes during Tropical Cyclone Olwyn. *J. Phys. Oceanogr.*, **49**, 1369–1379, https://doi.org/10.1175/JPO-D-18-0261.1.

Wang, G., and X. Zheng, 2016: Very large scale motions in the atmospheric surface layer: A field investigation. *J. Fluid Mech.*, **802**, 464–489, https://doi.org/10.1017/jfm.2016.439.

Wu, L., T. Hristov, and A. Rutgersson, 2018: Vertical profiles of wave-coherent momentum flux and velocity variances in the marine atmospheric boundary layer. *J. Phys. Oceanogr.*, **48**, 625–641, https://doi.org/10.1175/JPO-D-17-0052.1.

Yang, H., and T. Bo, 2018: Scaling of wall-normal turbulence intensity and vertical eddy structures in the atmospheric surface layer. *Bound.-Layer Meteor.*, **166**, 199–216, https://doi.org/10.1007/s10546-017-0306-6.

Zhao, R., and A. J. Smits, 2007: Scaling of the wall-normal turbulence component in high-Reynolds-number pipe flow. *J. Fluid Mech.*, **576**, 457–473, https://doi.org/10.1017/S0022112006004526.

Zou, Z., D. Zhao, B. Liu, J. A. Zhang, and J. Huang, 2017: Observation-based parameterization of air-sea fluxes in terms of wind speed and atmospheric stability under low-to-moderate wind conditions. *J. Geophys. Res. Oceans*, **122**, 4123–4142, https://doi.org/10.1002/2016JC012399.

——, ——, J. A. Zhang, S. Li, Y. Cheng, H. Lv, and X. Ma, 2018: The influence of swell on the atmospheric boundary layer under nonneutral conditions. *J. Phys. Oceanogr.*, **48**, 925–936, https://doi.org/10.1175/JPO-D-17-0195.1.

——, J. Song, P. Li, J. Huang, J. A. Zhang, Z. Wan, and S. Li, 2019: Effects of swell waves on atmospheric boundary layer turbulence: A low wind field study. *J. Geophys. Res. Oceans*, **124**, 5671–5685, https://doi.org/10.1029/2019JC015153.

——, S. Li, J. Huang, P. Li, J. Song, J. A. Zhang, and Z. Wan, 2020: Atmospheric boundary layer turbulence in the presence of swell: Turbulent kinetic energy budget, Monin–Obukhov similarity theory, and inertial dissipation method. *J. Phys. Oceanogr.*, **50**, 1213–1225, https://doi.org/10.1175/JPO-D-19-0136.1.